Seasonal Changes in Dense Water Production Do Not Cause Seasonal Cycle in Atlantic Overturning

D. GWYN EVANS,[a] OLIVER J. TOOTH,[a,b] MARTHA W. BUCKLEY,[c] N. PENNY HOLLIDAY,[a] AND SHELDON BACON[a,d,e]

[a] *National Oceanography Centre, Southampton, United Kingdom*
[b] *Department of Earth Sciences, University of Oxford, Oxford, United Kingdom*
[c] *Department of Atmospheric, Oceanic and Earth Sciences, George Mason University, Fairfax, Virginia*
[d] *University of Bangor, Bangor, United Kingdom*
[e] *University of Southampton, Southampton, United Kingdom*

(Manuscript received 10 March 2025, in final form 27 March 2026, accepted 1 May 2026)

ABSTRACT: The overturning circulation in the subpolar North Atlantic and Nordic seas is the product of a net densification by air–sea buoyancy forcing and mixing that transforms light Atlantic Water into dense North Atlantic Deep Water. Recent studies have shown that the magnitude of the time-mean overturning circulation as measured at the Overturning in the Subpolar North Atlantic Program (OSNAP) mooring array can be attributed to the water mass transformation by air–sea fluxes and mixing to the north of the array. However, connecting subpolar overturning variability on seasonal time scales to seasonal variations in water mass transformation is contentious. Here, we show in observations and a state estimate that seasonal variability in water mass transformation by air–sea buoyancy fluxes and mixing predominantly affects the storage of water in water mass classes within the subpolar basins, rather than driving seasonal changes in the overturning circulation at the OSNAP mooring array. Furthermore, we show that the seasonal formation and export of dense water from the Irminger and Labrador Seas cannot fully explain overturning seasonality at OSNAP. Instead, the seasonal cycle of overturning as measured at the OSNAP mooring array is the result of seasonal imbalances in the inflows and outflows of dense water across the array, linked to seasonal changes in the density field imprinted on the circulation of the subpolar gyre. This implies that intra-annual-to-seasonal dense water transport variability at OSNAP cannot be interpreted as an overturning circulation associated with the formation and export of dense water.

KEYWORDS: Fluxes; Mass fluxes/transport; Meridional overturning circulation; Ocean circulation; Inverse methods; Seasonal variability

1. Introduction

In the subpolar North Atlantic, warm, salty, and light waters of subtropical origin are made cooler and fresher but ultimately denser by air–sea buoyancy fluxes and mixing (Xu et al. 2018; Berglund et al. 2023; Buckley et al. 2023; Evans et al. 2023). As part of the Atlantic meridional overturning circulation (AMOC), this diapycnal water mass transformation produces North Atlantic Deep Water (NADW) that fills the deep interior of the Atlantic Ocean. Deep waters are eventually upwelled in the Southern Ocean (Marshall and Speer 2012). Dense water formation plays a key role in the sequestration of excess anthropogenic heat and carbon dioxide, mitigating the impact of climate change (IPCC 2021). Seasonal-to-interannual variations in the meridional transports of heat and freshwater associated with the AMOC may impact sea surface temperature and salinity, with important implications for European weather (Duchez et al. 2016; Oltmanns et al. 2020).

According to the water mass transformation framework described by Walin (1982), the diapycnal water mass transformation by air–sea buoyancy fluxes and mixing within a domain is equivalent to the diapycnal overturning streamfunction measured at the boundary of the domain. Analysis using data from the Overturning in the Subpolar North Atlantic Program (OSNAP; Lozier et al. 2017, 2019) mooring array has revealed that in the time mean, cooling by air–sea buoyancy fluxes transforms light Atlantic Waters into subpolar mode water, and mixing between and Atlantic Water and Arctic Water further cools and freshens Atlantic Water. NADW is mainly formed by mixing of subpolar mode waters, intermediate waters, and overflow waters originating in the Nordic seas (Evans et al. 2023; Zou et al. 2024). These results complement the existing and ongoing body of work in the subpolar North Atlantic that address the mechanisms of air–sea buoyancy forcing and mixing in relation to water mass transformation (Brambilla et al. 2008; Stendardo et al. 2024; Spall and Pickart 2001; Spall 2003, 2004; Straneo 2006; Fer et al. 2010; Beaird et al. 2012; Brüggemann and Katsman 2019; Xu et al. 2018; Le Bras et al. 2020; Petit et al. 2020; Dey et al. 2024; Stendardo et al. 2024).

Denotes content that is immediately available upon publication as open access.

Supplemental information related to this paper is available at the Journals Online website: https://doi.org/10.1175/JPO-D-25-0053.s1.

Corresponding author: D. Gwyn Evans, dgwynevans@noc.ac.uk

DOI: 10.1175/JPO-D-25-0053.1

However, understanding the impact of time-varying air–sea buoyancy fluxes and mixing on the diapycnal overturning as measured at OSNAP is more challenging. For example, Petit et al. (2020) show that the seasonal cycle of water mass transformation by air–sea buoyancy fluxes in the Irminger Sea (IS) and Iceland Basin (IB) far exceeds the seasonality of the overturning measured at OSNAP, as anticipated by the theoretical work of Marshall et al. (1999). Several studies have found that the variability and export of dense water from the subpolar North Atlantic do not reflect the rate at which dense water is formed due to the subbasin- and basin-scale recirculation of dense water in the subpolar gyre (Dengler et al. 2006; Fischer et al. 2010; Zantopp et al. 2017; Handmann et al. 2018). As a result of these recirculations, the residence time in the subpolar gyre (decadal) is much longer than typical time scales of dense water formation (MacGilchrist et al. 2021; seasonal). The consequence is that on shorter time scales, dense water formation affects the storage of dense water in the Irminger Sea and Labrador Sea (LS) as opposed to the diapycnal overturning (Buckley et al. 2023). As such, only interannual-to-decadal water mass transformation results in changes in overturning (Marsh 2000; Brambilla et al. 2008; Desbruyères et al. 2019; Årthun 2023), where the time scale of air–sea buoyancy forcing variability exceeds that of the residence time of water in the subpolar North Atlantic.

A recent study by Fu et al. (2023) shows that the seasonal cycle of overturning at OSNAP lags that of the surface-forced water mass transformation by 5 months, with dense water formation peaking in January and the overturning peaking in May. Their analysis does not go further in determining whether the export of the dense water (i.e., transport southward across the OSNAP mooring array in the East Greenland Current and Labrador Current) that is formed in January drives a peak in the overturning in May, where the delay is associated with the transit time of the newly formed dense water from its formation site to the OSNAP mooring array. However, they do show that the seasonal cycle of water mass transformation by air–sea buoyancy fluxes is ~3 times the seasonal range in the overturning at OSNAP, implying that seasonal water mass transformation is balanced by storage rather than export in accord with previous studies. Previous work at OSNAP has found no discernible relationship between seasonal dense water formation and export across the OSNAP mooring array (Li et al. 2021), and model-based analyses have further highlighted this disconnect (Fox et al. 2025). However, as also discussed in Fu et al. (2023), a recent analysis of the export of dense water formed in the Irminger Sea finds that some seasonally formed dense water is exported within the East Greenland Current within 3 months of its formation and may imprint on the seasonal cycle of the diapycnal overturning at the eastern OSNAP mooring array (Le Bras et al. 2020). Indeed, based on the transport variability across the OVIDE hydrographic section between Portugal and Greenland, Mercier et al. (2024) speculate that this lagged export of dense water drives seasonal density changes in the East Greenland Current, leading to the observed seasonal peak in overturning. Similarly, Tooth et al. (2023b) and Wang et al. (2021) find that seasonal density changes in the Irminger Sea drive the seasonal cycle of overturning in an ocean model and reanalysis, respectively.

Prior literature clearly demonstrates that the seasonal cycle of water mass transformation exceeds that of export, and on average, waters have long (decadal) residence times in the subpolar gyre. However, it is possible that some waters are exported more rapidly, allowing the seasonal cycle of water mass transformation to drive a seasonal cycle in export. As a result, we reexamine the seasonal variability of water mass transformation by air–sea buoyancy fluxes and mixing in the subpolar North Atlantic using observations and a state estimate. We will then determine how this water mass transformation impacts the overturning as measured at the OSNAP mooring array in terms of the export of dense water from the Irminger Sea and the Labrador Sea.

2. Methods

We begin by describing the water mass transformation framework used to relate dense water export and overturning variability at OSNAP to dense water formation by air–sea buoyancy forcing and mixing in the region to the north of the OSNAP mooring array. We then describe the datasets used to calculate each of the terms in this water mass transformation framework.

a. The water mass transformation framework

The rate of change in the volume V of water between two tracer surfaces can be related to the diasurface transformation G of water across the tracer isosurfaces (Walin 1982). If the domain in question is bound by a fixed open section, then V also depends on the transport of water M into the domain between the two tracer surfaces (i.e., $C^* \pm \Delta C/2$), so that

$$\frac{dV(C^*, t)}{dt} = M + \frac{\partial G(C^*, t)}{\partial C}, \tag{1}$$

where C is a generic tracer and * denotes the tracer isosurface. Further, the diasurface transformation G can be separated into the contributions by air–sea exchange E, where tracer surfaces outcrop at the sea surface, and mixing F which is calculated as a residual:

$$G(C^*, t) = E(C^*, t) + F(C^*, t). \tag{2}$$

As described in Evans et al. (2023), this framework can, therefore, be used to quantify how air–sea buoyancy fluxes and mixing contribute to the magnitude of the overturning in density, temperature, and salinity space. Here, we use the methods outlined in Evans et al. (2023) to relate the variability of the overturning as measured at the OSNAP mooring array (i.e., M) to the water mass transformation by air–sea buoyancy fluxes E and mixing F, with a particular focus on seasonal time scales. We focus on the region to the north of the OSNAP mooring array, including the subpolar North Atlantic, the Nordic seas, and the Arctic Ocean. As in Evans et al. (2023), we do not consider the transport through the Bering Strait in our analysis, which in this context we consider to be negligible.

b. Data sources

This analysis uses an observational-based combination of datasets and an ocean state estimate to relate the variability of the overturning at the OSNAP mooring array to the water mass transformation by air–sea buoyancy fluxes and mixing. In both datasets, to calculate the volume, V, and the water mass transformation, G, we use gridded fields of temperature Θ and salinity S binned into density, temperature, and salinity space. The calculation of the water mass transformation by air–sea buoyancy fluxes, E, requires gridded fields of surface net heat and freshwater fluxes, while the water mass transformation implied by the overturning, M, is calculated using gridded fields of temperature, salinity, and velocity along the OSNAP mooring array which forms the boundary of our domain. The residual term, F, is then calculated by subtracting the overturning, M, and the air–buoyancy forcing, E, from the water mass transformation, G, giving the water mass transformation in G that is not explained by air–sea buoyancy forcing and transport of water in/out of our domain. In the water mass transformation framework, this residual transformation, F, is interpreted as the water mass transformation due to mixing, but in the observations, it also includes errors linked to instrumentation, sampling, and interpolation.

The observational-based combination of datasets is made up of EN4, ARMOR3D, ERA5, NCEP CFSv2, JRA-55, and OSNAP. Using these datasets, volume V and transformation G are calculated using EN4 and ARMOR3D. The water mass transformation by air–sea buoyancy fluxes E is calculated using air–sea fluxes from ERA5, NCEP CFSv2, and JRA-55, and surface Θ and S are calculated from EN4 and ARMOR3D. Further, the overturning M is calculated using data from the OSNAP mooring array. The residual term F is then calculated using the six combinations of these datasets, e.g., EN4/ERA5/OSNAP and EN4/NCEP CFSv2/OSNAP. The volume and water mass transformation shown for the observations, therefore, represent a mean of these dataset combinations, and their standard deviation provides a measure of uncertainty in our final results.

From EN4 and ARMOR3D, we use gridded fields of Θ and S. EN4 is an objective analysis of all available subsurface Θ and S profiles, resulting in monthly gridded fields with 1° horizontal resolution and 42 irregularly spaced depth levels. We use version EN4.2.2 with the bias correction g10, downloaded on 29 January 2024 (Good et al. 2013). ARMOR3D is a multi-observational (Θ and S profiles, satellite-altimeter-based sea level anomaly and satellite-based sea surface temperature fields) analysis, providing monthly fields of Θ and S with a horizontal resolution of 0.25° and 50 irregularly spaced depth levels (Guinehut et al. 2012). These observational-based products have been used to study water mass properties and variability in the subpolar North Atlantic and Nordic seas (Broomé et al. 2020; Holliday et al. 2020; Kenigson and Timmermans 2021; Verezemskaya et al. 2021; Evans et al. 2023; Årthun et al. 2025).

From ERA5, we use surface latent heat flux, surface sensible heat flux, surface net solar radiation, surface net thermal radiation, evaporation, and total precipitation, at a monthly resolution and a 0.25° horizontal resolution (Hersbach et al. 2021). From NCEP CFSv2, we use downward longwave radiation flux, upward longwave radiation flux, downward shortwave radiation flux, upward shortwave radiation flux, sensible heat flux, latent heat flux, and evaporation minus precipitation (Saha et al. 2012). We use monthly mean NCEP CFSv2 data with a 0.5° horizontal resolution. From JRA-55, we use the monthly mean model two-dimensional average diagnostic fields for latent heat flux, sensible heat flux, downward longwave radiation flux, upward longwave radiation flux, downward solar radiation flux, upward solar radiation flux, evaporation, and total precipitation (JMA 2013) with a horizontal resolution of ~0.5°.

For the calculation of the water mass transformation implied by the overturning M, we use observational-based gridded fields of Θ, S, and cross-sectional velocity from the OSNAP mooring array. The OSNAP mooring array was deployed between Newfoundland and Greenland and from Greenland to Scotland in August 2014, and data are currently available up to June 2022 (Fu et al. 2025). The OSNAP data are averaged into 30-day bins. All of the observational-based data described above are selected to span the same time period as the OSNAP time series.

The ocean state estimate used here is the Estimating the Circulation and Climate of the Ocean, version 4 release 4 (ECCOv4r4). We use monthly three-dimensional fields (~1° horizontal resolution) of Θ, S, velocity, bolus velocity, net heat flux, and net freshwater flux (Forget et al. 2015; Fukumori et al. 2021; ECCO Consortium et al. 2021). In ECCOv4r4, we calculate the transport across a section of the model grid that matches the location of the OSNAP mooring array. ECCOv4r4 uses an adjoint model to determine the optimal combination of ocean model initial conditions, model parameters, and atmospheric boundary conditions to give the best agreement between model output and observations in a kinematically and dynamically consistent way. ECCOv4r4, therefore, ultimately uses the same observational data sources as EN4 and ARMOR3D; however, the application differs. In contrast to reanalysis products based upon sequential methods, adjoint-based ECCOv4r4 estimates are free of artificial internal heat and freshwater sources/sinks and fulfill known conservation laws exactly. As a result, the volume budget characterized by the water mass transformation framework will balance exactly.

In both the observations and ECCOv4r4, we calculate density as the potential density anomaly referenced to 0 dbar (σ), using the Thermodynamic Equation of Seawater 2010 (IOC et al. 2010) and 1980 International Equation of State, respectively. Therefore, in the observations, Θ and S represent Conservative Temperature and Absolute Salinity, respectively. In ECCOv4r4, Θ and S represent potential temperature and practical salinity, respectively. We calculate the temporal variability of the diapycnal overturning at a time-varying density of maximum overturning, so that

$$\mathrm{MOC}(t) = \max[M(\sigma^*, t)] = \max\left[\int_{\sigma_{\max}}^{\sigma}\int_{x_w}^{x_e} \upsilon(x, \sigma^*, t)\,dx\,d\sigma\right], \tag{3}$$

where υ is the velocity normal to the OSNAP section. The x_w and x_e are the western and eastern limits of the integration,

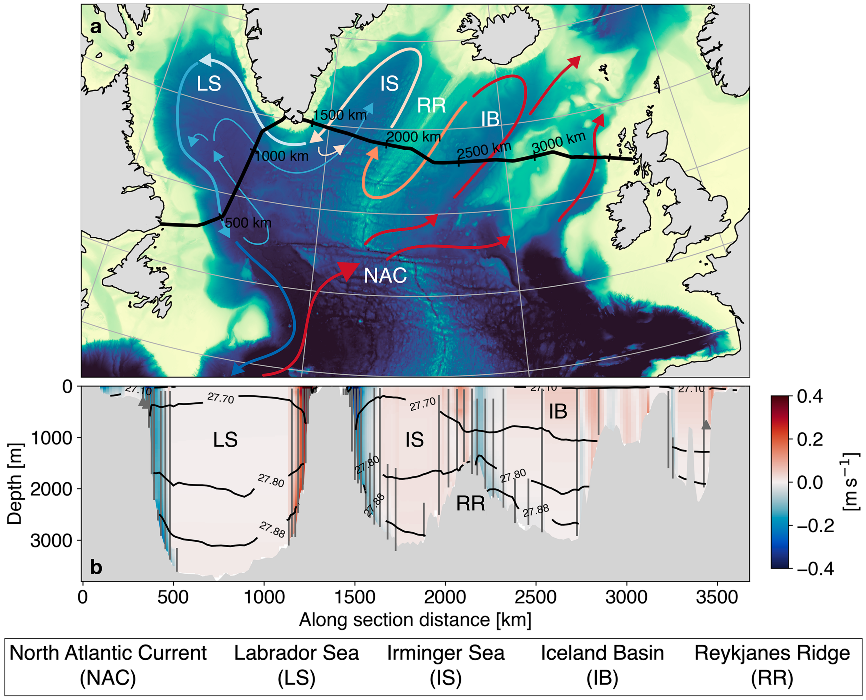

FIG. 1. Subpolar North Atlantic circulation and OSNAP velocity. (a) A schematic representation of the circulation in the subpolar North Atlantic, showing the northward-flowing NAC, and the progressive cooling and densification (represented by the arrow color) of Atlantic Water as it circulates around the IB, the RR, the IS, and the LS. The black line shows the location of the OSNAP mooring array, with the along-section distance from the Labrador Coast marked. (b) Time mean of the velocities normal to the OSNAP mooring array from observations (2014–20), with positive values indicating northward flow across the array. The black contours show isopycnal surfaces of σ, and the vertical gray lines and triangle markers indicate the positions of the OSNAP moorings.

which extend from Labrador to Scotland for the full OSNAP section, from Labrador to Greenland for the western portion of the OSNAP section, and from Greenland to Scotland for the eastern portion of the OSNAP section.

3. Results

a. Water mass transformation in the subpolar North Atlantic and Nordic seas

In this section, we will assess the role of air–sea forcing and mixing in driving seasonal changes in the overturning variability at the OSNAP mooring array. Ultimately, we aim to determine if seasonal changes in dense water export drive seasonal changes in the diapycnal overturning at OSNAP. It is, therefore, useful to first assess how the basin-scale circulation and density structure of the subpolar North Atlantic imprints on the velocity and density along the OSNAP mooring array and how this ultimately manifests as an overturning at OSNAP.

Warm, salty, and light Atlantic water enters the subpolar North Atlantic along the North Atlantic Current (NAC, Fig. 1a). Along its path through the subpolar basins, Atlantic Water is gradually cooled and freshened, forming subpolar mode water and ultimately Labrador seawater. Combined, Labrador seawater and dense overflow water (originating from north of the Greenland–Scotland Ridge) form NADW. The velocity normal to the OSNAP mooring array (Fig. 1b) reveals a complex flow pattern consisting of a broad area of northward flowing light (and warm) Atlantic Water between the Iceland Basin and Scotland (2500-km distance ordinate to the eastern end of the OSNAP array) fed by the NAC. To the west of the NAC is a series of topographically bound inflows and outflows along the Reykjanes Ridge (RR) and around the continental margins of Greenland and Labrador/Newfoundland. In addition, there are weaker recirculations to the east of the Labrador Current and the East Greenland Current, where the former is resolved only by one mooring near the 500-km distance ordinate (Lavender et al. 2000; Våge et al. 2011; Handmann et al. 2018). These recirculations are likely wind driven but modulated by the stratification in the subpolar gyre, topographic effects, and eddy fluxes (Spall and Pickart 2003).

In the eastern subpolar basin, between Greenland and Scotland, the shoaling of isopycnals from east to west results from the increase in the proportion of dense (and cold) water outflows compared to the light (and warm) water inflows. Consequently, light and warm water is predominantly imported northward across OSNAP east, while dense and cold water is exported southward. In the Labrador Sea (OSNAP west),

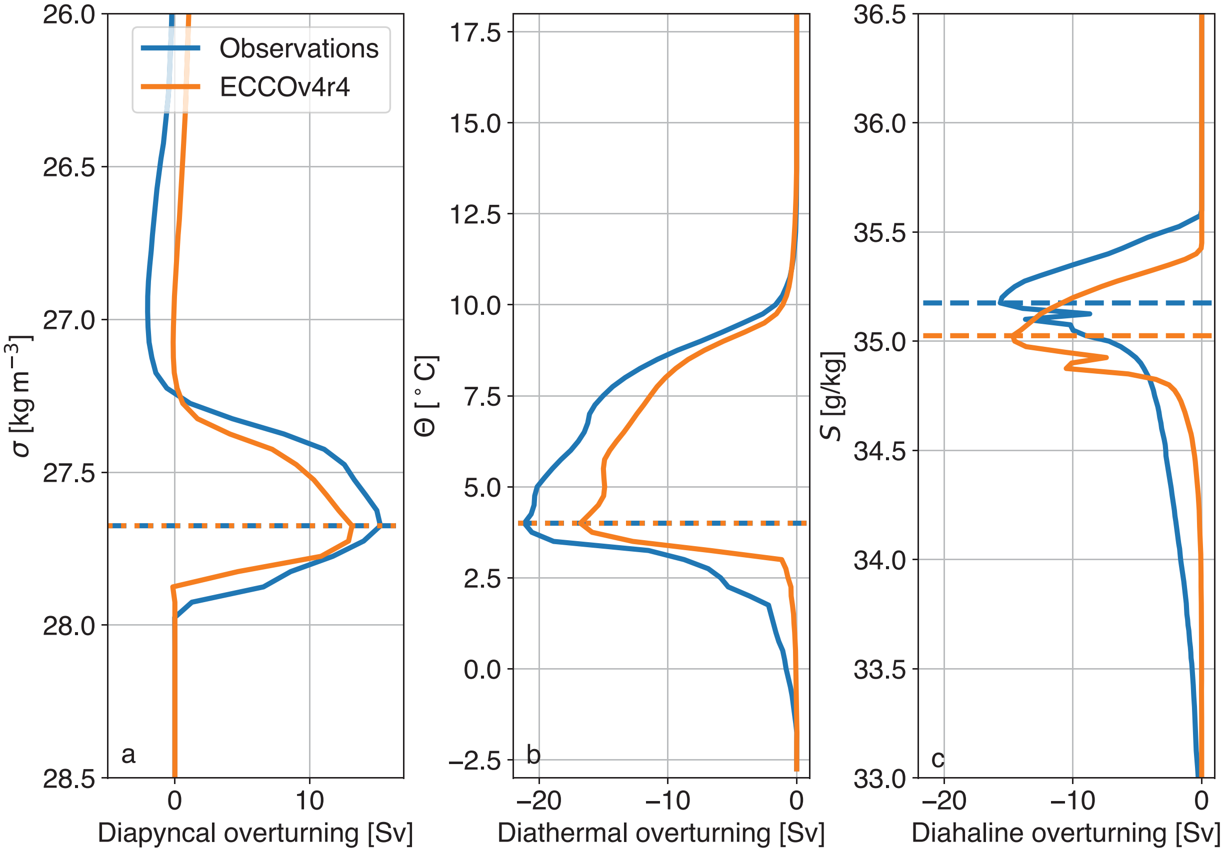

FIG. 2. Overturning in the subpolar North Atlantic. (a) Diapycnal overturning streamfunction calculated along the observed OSNAP section (blue) and the equivalent section in ECCOv4r4 integrated from dense to light. (b) Diathermal overturning streamfunction calculated along the observed OSNAP section (blue) and the equivalent section in ECCOv4r4. (c) Diahaline overturning streamfunction calculated along the observed OSNAP section (blue) and the equivalent section in ECCOv4r4. The dashed lines show the respective tracer value at the maximum magnitude of the overturning.

the water that flows southward across OSNAP in the Labrador Current is denser (cooler and fresher) than the water that flows in via the West Greenland Current. However, this contrast in density is much less than that in the eastern basin, resulting in a weaker diapycnal overturning across OSNAP west (Lozier et al. 2019).

The contrast in the density, temperature, and salinity of water entering the subpolar North Atlantic across the OSNAP array versus the density, temperature, and salinity of the water exported from the subpolar North Atlantic can be used to derive the overturning streamfunction in density, temperature, and salinity space (Fig. 2; Evans et al. 2023). The strength of the observed and modeled overturning in density, temperature, and salinity space is the maximum of the overturning streamfunction with time-mean values of 15.11, 20.76, and 15.74 Sv (1 Sv ≡ 10^6 m^3 s^{-1}) at 27.675 kg m^{-3}, 4.00°C, and 35.18 g kg^{-1} in the observations and 13.16, 16.80, and 14.68 Sv at 27.675 kg m^{-3}, 4.00°C, and 35.03 in ECCOv4r4 (Fig. 2). While the overturning in tracer coordinates is weaker in ECCOv4r4 compared with observations, this does not prevent us from using ECCOv4r4 as a tool to understand how seasonal water mass transformations may impact overturning. Given that ECCOv4r4 is a physically and dynamically consistent framework, we can, therefore, more definitively quantify the relative roles of water mass transformation and storage in setting the variability of the diapycnal overturning in the state estimate to help us better understand the observations.

While the structure and magnitude of the time-mean overturning streamfunction is set by the time-mean transformation by air–sea buoyancy fluxes and mixing (Evans et al. 2023), variability of the diapycnal overturning streamfunction [i.e., M in Eq. (1); Figs. 3e,f] differs from that of the water mass transformation by air–sea buoyancy fluxes [i.e., E in Eq. (2); Figs. 3c,d] and mixing [i.e., F in Eq. (2); Figs. 3g,h]. Instead, the variability of air–sea buoyancy fluxes and mixing drives changes in the volume of water in density classes north of the OSNAP mooring array [i.e., G in Eq. (1); Figs. 3a,b; see also Buckley et al. 2023]. For example, in both the observations (Fig. 3, left column) and ECCOv4r4 (Fig. 3, right column), the variability of the diapycnal water mass transformation by air–sea buoyancy fluxes and mixing is dominated by the seasonal cycle, with densification and cooling during the winter

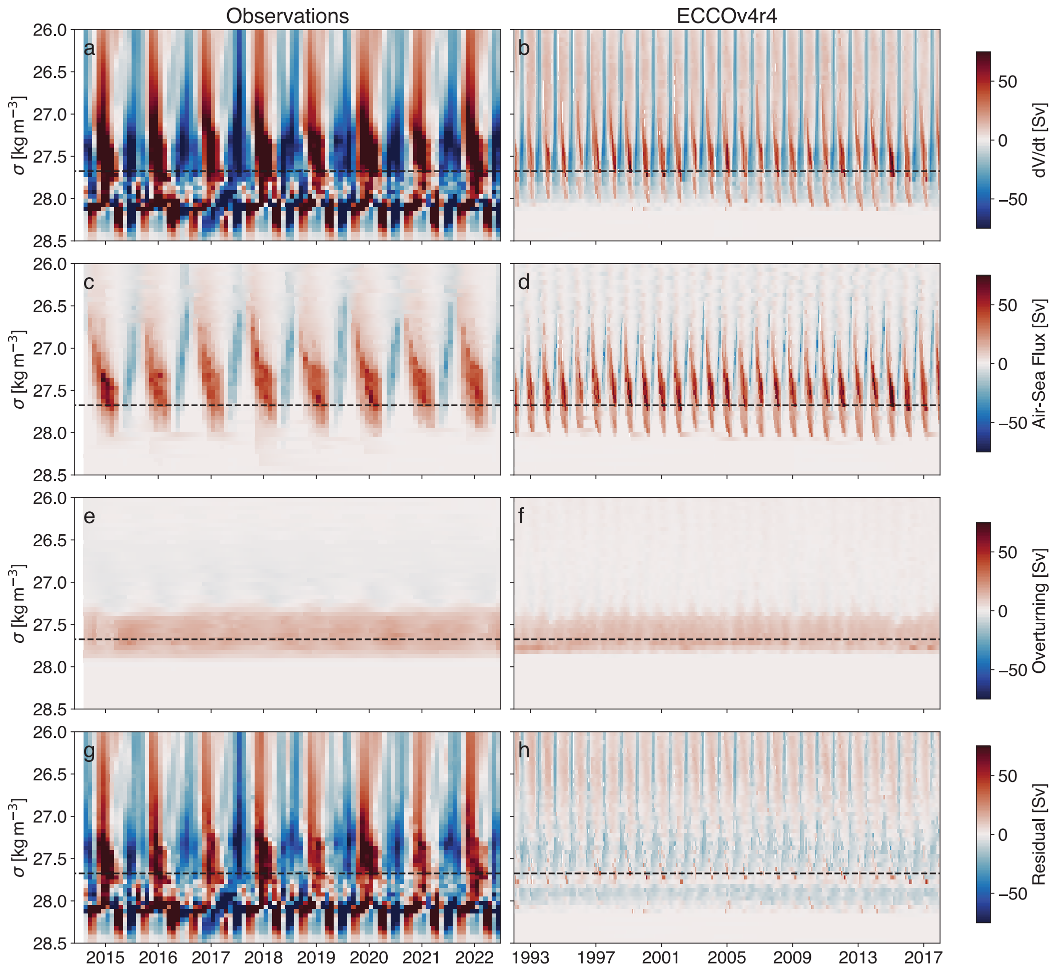

FIG. 3. Subpolar North Atlantic water mass transformation in density space. (left) Water mass transformation calculated from the observational dataset combination and (right) water mass transformation from ECCOv4r4. (a),(b) The transformation of water derived from the volume change, i.e., the storage of water north of OSNAP, where a positive transformation implies densification. (c),(d) The water mass transformation by air–sea buoyancy forcing. (e),(f) The overturning streamfunction. (g),(h) The residual water mass transformation that we attibute to mixing. The dashed black line marks the density of the maximum of the mean overturning streamfunction.

and lightning and warming during the summer. In contrast, the range in variability of the diapycnal overturning streamfunction is much less. Therefore, the transformation of water by air–sea buoyancy fluxes and mixing affects the storage of water in density classes and does not produce an equivalent response in the export of water from the region north of the OSNAP mooring array.

The comparison between the observations and ECCOv4r4 in Fig. 3 also highlights differences between the water mass transformation calculated using the observations and ECCOv4r4. For example, in the observations, dV/dt (representing the storage of water in density classes) has a larger range compared to ECCOv4r4 and is generally noisier, particularly at higher densities. In contrast, the variability of the air–sea flux and overturning terms is similar in the observations and ECCOv4r4. As a result, the residual term, calculated by subtracting the overturning and air–sea flux terms from the dV/dt term, is also different in the observations and ECCOv4r4. The larger variability in the dV/dt term in the observations is likely caused by errors linked to instrumentation, sampling, and the interpolation of the gridded Θ and S fields and, for the residual term, by mismatches between the data products used in the calculation. While ECCOv4r4 may not exactly simulate the variability of the diapycnal overturning at the OSNAP mooring array, we can be confident that the physical and dynamical consistency of ECCOv4r4 reduces the impact of such errors and allows us to close the volume budget (Evans et al. 2017; Heimbach et al. 2019). ECCOv4r4 clearly demonstrates that seasonal variations in air–sea buoyancy forcing and mixing impact the storage of water in density classes as opposed to the diapycnal overturning. Hereinafter, we will, therefore, only show the storage and residual terms using data from ECCOv4r4.

Seasonal water mass transformation by air–sea buoyancy forcing and mixing to the north of the OSNAP mooring array,

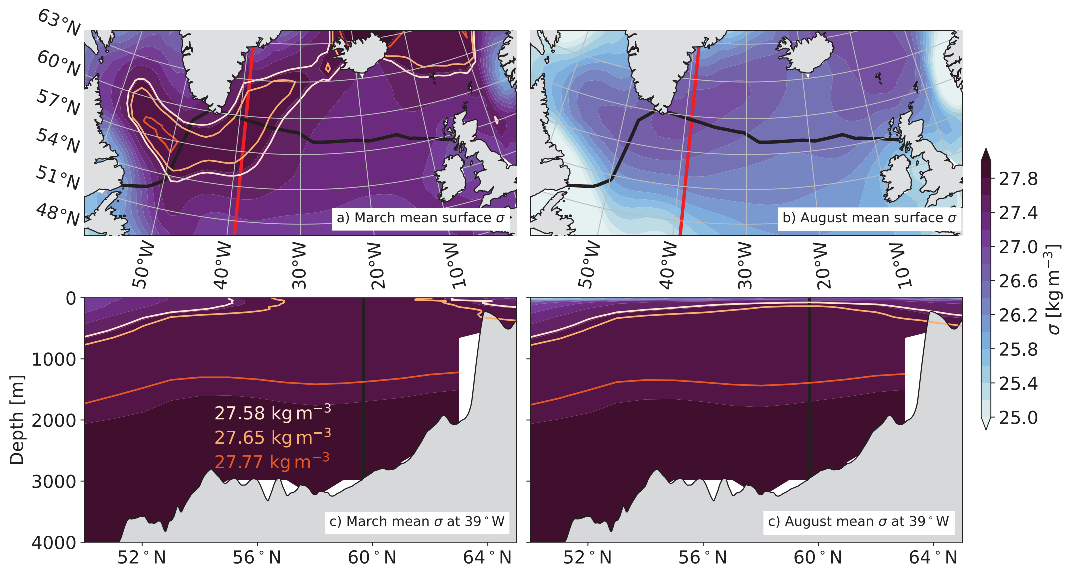

FIG. 4. Seasonal isopycnal outcrop variability in the subpolar North Atlantic. (a) March and (b) August mean (2010–22) surface density in EN4.2.2 showing the outcropping area for σ = 27.58 kg m^{-3}, σ = 27.65 kg m^{-3}, and σ = 27.77 kg m^{-3}. (c),(d) Depth sections along the red lines are shown for the respective months. The black lines indicate the position of the OSNAP mooring array.

therefore, predominantly leads to changes in the storage of water within density classes, rather than driving seasonal changes in the diapycnal overturning at OSNAP with a similar magnitude. This decoupling between seasonal water mass transformation and overturning is evident in the seasonal outcropping of isopycnals in the subpolar North Atlantic (Fig. 4). This shows that the large changes in isopycnal outcrop area at the sea surface (Figs. 4a,b) generally only impact the vertical density structure in the upper 500 m and in the interior of the subpolar basins (Figs. 4c,d). The seasonal cycle of wintertime densification and summertime lightning, therefore, acts on water predominantly shallower than 500 m. In these regions and at these depths, the export time scale of seasonally formed dense water means that this dense water is re-entrained by the seasonal "demon" as described in MacGilchrist et al. (2021), so that on a seasonal basis, the same water is transformed between density classes. In addition, Fig. 4 highlights how the OSNAP mooring array intersects the regions where dense water isopycnals outcrop in the Irminger and Labrador Seas and, therefore, where dense water forms. This implies that local seasonal changes of density and dense water formation may impact the seasonal transport variability, in addition to the advective propagation of any remote density anomalies.

b. *Seasonal overturning and water mass transformation*

In the previous section, we showed that the seasonal water mass transformation by air–sea buoyancy forcing and mixing does not drive a seasonal diapycnal overturning at OSNAP with a similar magnitude. In this section, we will examine this disconnect in more detail, by assessing the structure of the seasonal cycle in density space and by examining the lagged correlation between the water mass transformation and the diapycnal overturning.

The seasonal cycle of the diapycnal overturning and water mass transformation further reveals the contrast between the large seasonality of the water mass transformation by air–sea buoyancy fluxes and the weaker seasonality of the overturning at OSNAP in both the observations and ECCOv4r4 (Fig. 5). The seasonal cycle of the diapycnal overturning at the density of maximum overturning in the observations and ECCOv4r4 has amplitudes of ~6 and ~4.5 Sv, peaking in April and May, respectively. This is compared to the seasonal cycle of the water mass transformation by air–sea buoyancy fluxes that has an amplitude of >50 Sv, peaking in January (observations) and February (ECCOv4r4). In ECCOv4r4, dV/dt has a seasonal amplitude of ~65 Sv and peaks in February/March and the residual term has a seasonal amplitude of ~17 Sv with a peak in March.

Focusing on ECCOv4r4, profiles of water mass transformation in density space (Figs. 5c–f) highlight that across all densities, the seasonal cycle of air–sea buoyancy forcing leads to changes in the seasonal cycle of dV/dt, as opposed to the diapycnal overturning. Further, the phase and structure of these seasonal cycles in density space (i.e., air–sea buoyancy forcing and overturning) are different. In both the observations and ECCOv4r4, the large seasonality in the water mass transformation by air–sea buoyancy fluxes and mixing, therefore, does not drive a seasonal cycle in the overturning with a similar magnitude and timing. Instead, the volume change or storage in density classes (Fig. 5b, red line) changes to reflect the seasonal cycle of air–sea buoyancy fluxes and mixing.

While we show above that the seasonality of water mass transformation by air–sea buoyancy fluxes and mixing exceeds the seasonality of the overturning, it may be that some physically meaningful lagged correlation exists between the water mass

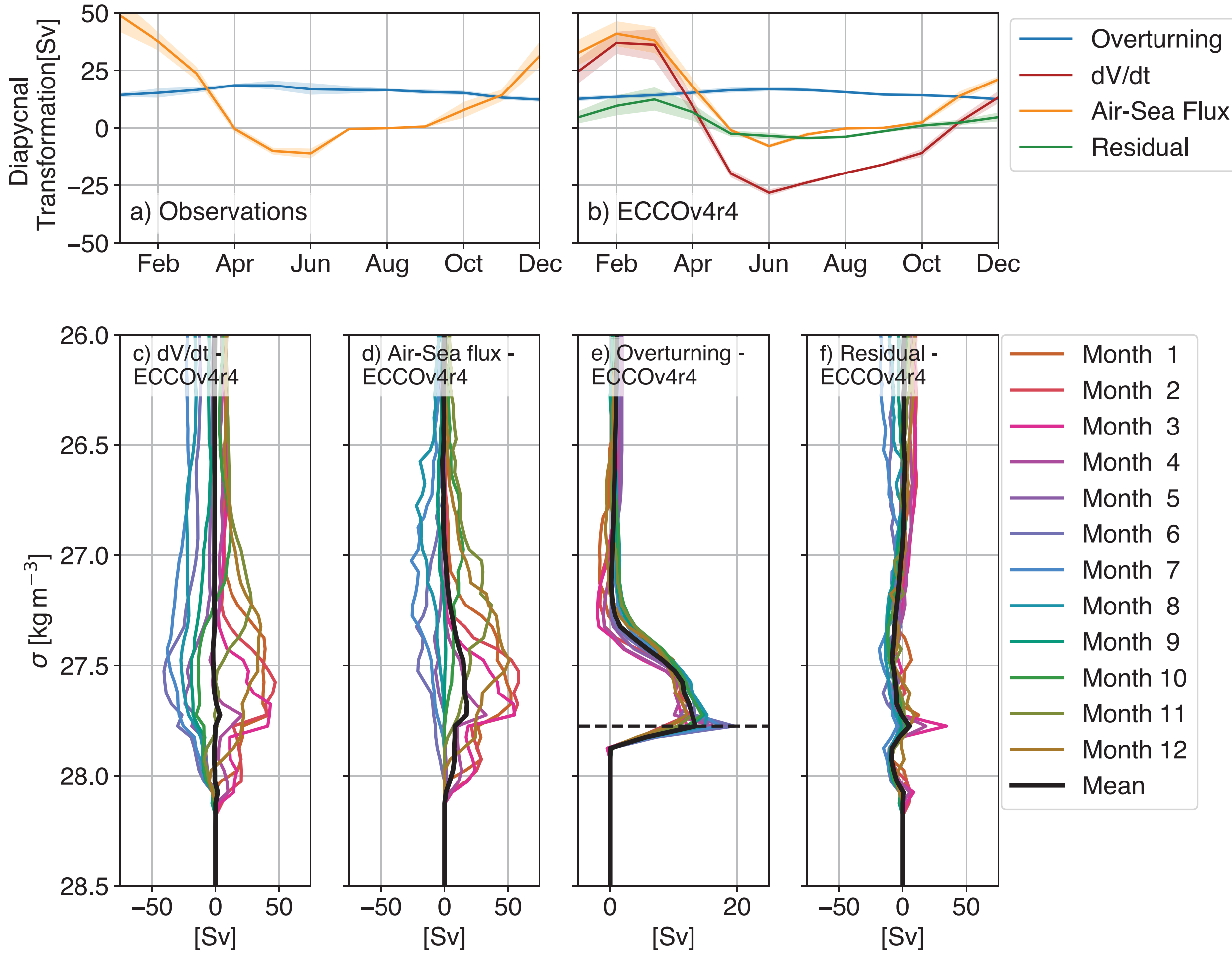

FIG. 5. Seasonal diapycnal overturning and water mass transformation. (a),(b) The seasonal cycle of the diapycnal overturning and the water mass transformation by air–sea buoyancy forcing at the density of maximum overturning for the observations and ECCOv4r4. For ECCOv4r4, the seasonal cycle of the storage and residual terms at the density of maximum overturning is also shown in (b). For the observations only, the monthly mean values are calculated using data from 2015 to 2021 inclusive. The colored shading shows the 90% confidence interval of the monthly mean determined using a Monte Carlo approach. Monthly mean profiles in density space calculated from ECCOv4r4, showing (c) the rate of change of volume or storage, (d) the water mass transformation by air–sea buoyancy fluxes, (e) the overturning streamfunction at OSNAP, and (f) the residual water mass transformation. The solid colored lines show individual months, and the thick solid black line shows the time mean. The dashed line shows the mean density of maximum overturning.

transformation and the overturning, as discussed in Fu et al. (2023). Indeed, an analysis of the lagged correlation between the time series of the maximum diapycnal overturning streamfunction and the transformation by air–sea buoyancy fluxes at all densities reveals a significant correlation where the air–sea buoyancy fluxes leads the overturning by 4–5 months across all densities (Fig. 6). One possible explanation for this lagged correlation, discussed in Fu et al. (2023), is the delay between the seasonal wintertime maximum in dense water formation within the subpolar basins and the export of this dense water across the OSNAP section in the East Greenland Current and the Labrador Current, where it is assumed that dense waters take 4–5 months to reach the OSNAP section from their formation regions. We will, therefore, test this hypothesis by examining the relationship between dense water formation, dense water export, and diapycnal overturning in the observations.

c. *The relationship between dense water formation, export, and overturning at OSNAP*

In this section, we examine whether rapid export of dense water in boundary currents can explain the correlation between transformation by air–sea buoyancy fluxes and the overturning (Fig. 6), despite the much larger seasonal cycle of the former (Fig. 5). To do this, we separately consider the eastern and western components of the OSNAP array and calculate the export within the boundary currents. We calculate water mass formation by air–sea buoyancy fluxes using ERA5. We consider dense waters between the mean density of maximum overturning ($\overline{\sigma}_{\mathrm{OV}}$) and $\sigma = 28.0\ \mathrm{kg\ m^{-3}}$, where $\overline{\sigma}_{\mathrm{OV}}$ is calculated separately for OSNAP east and west. When accumulated across the full width of the eastern and western OSNAP arrays, the transport of these dense waters should be

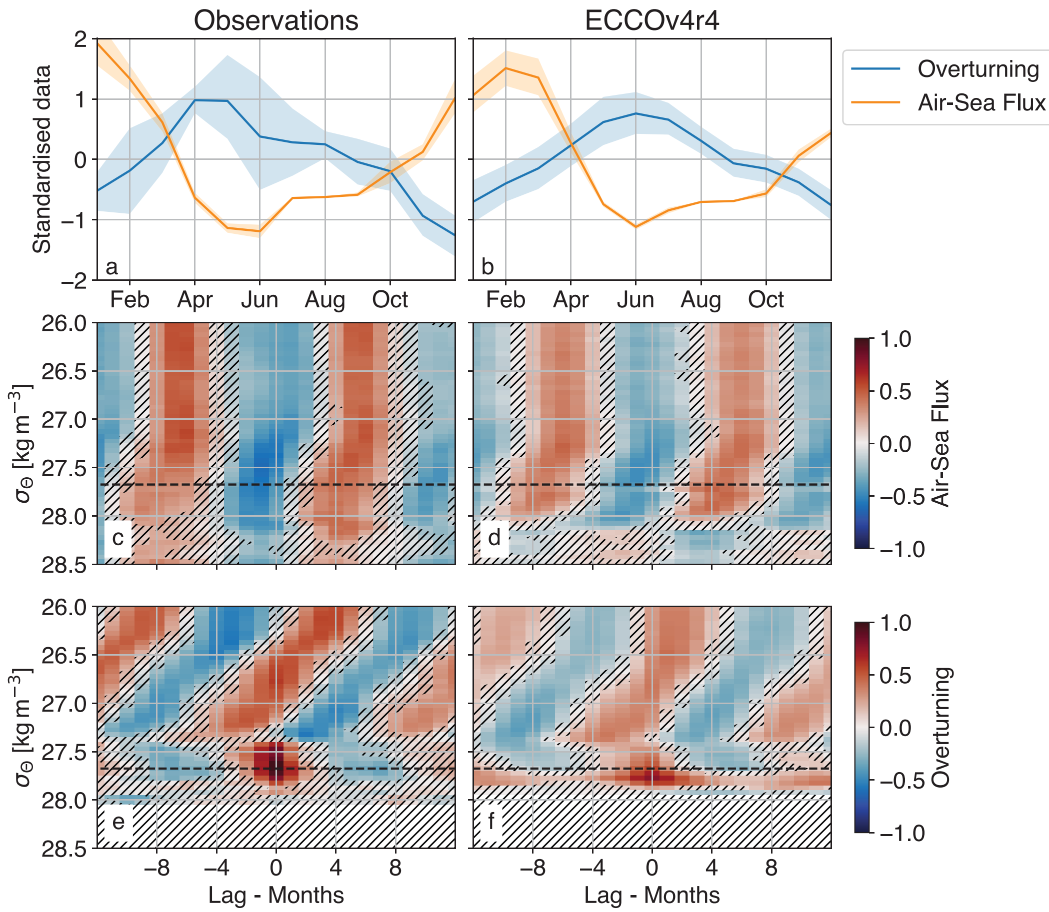

FIG. 6. Lagged correlation between the diapycnal overturning and water mass transformation. A comparison between the observational dataset combination and ECCOv4r4. The standardized (time-mean anomaly, divided by the standard deviation) seasonal cycle of the overturning streamfunction and the diapycnal air–sea buoyancy flux at the density of maximum overturning [(a) observations, (b) ECCOv4r4; the colored shading shows the 90% confidence interval of the monthly mean determined using a Monte Carlo approach]. The lagged correlation for the observations and ECCOv4r4 between the maximum of the diapycnal overturning streamfunction and the water mass transformation by (c),(d) air–sea buoyancy fluxes and (e),(f) the diapycnal overturning streamfunction at all densities. A positive (negative) value indicates that overturning lags (leads). The dashed black line shows the density of maximum overturning.

equivalent to the diapycnal overturning that we calculate by integrating meridional velocity from dense to light, except that we calculate the diapycnal overturning with a time-varying σ_{OV}.

We first consider the formation and export of dense water in the eastern OSNAP basin, focusing on water between the mean $\overline{\sigma}_{OV}^{east} = 27.575\,\mathrm{kg\,m^{-3}}$ and $\sigma = 28.0\,\mathrm{kg\,m^{-3}}$ (Figs. 7a,b). We calculate formation between the OSNAP east mooring array and the Greenland–Scotland Ridge. In this region, formation (dashed black line) peaks in January (Fig. 7b); previous studies have shown that these dense water classes are predominantly formed in the Irminger Sea (Petit et al. 2020). If the formation of this dense water leads to a lagged increase in the overturning, we would, therefore, expect to see a corresponding 4–5-month lagged peak in the dense water export within the East Greenland Current (EGC), the main outflow for dense water formed in the Irminger Sea, defined here as the section of southward transport between Greenland and 39.6°W (see the dashed vertical line in Figs. 2a and 3a in the online supplemental material).

However, to fully account for the variability and seasonal cycle of the overturning at OSNAP east (solid black line, Figs. 7a,b), the dense water volume transport (between $\overline{\sigma}_{OV}^{east}$ and $\sigma = 28.0\,\mathrm{kg\,m^{-3}}$) must be integrated across the full extent of the OSNAP east mooring array (red line, Figs. 7a,b) not just the EGC (red line, Figs. 7a,b). Further, the seasonal maximum of dense water export in the EGC (blue line, Fig. 7a) can be seen clearly in January/February each year, lagging the peak in the formation by air–sea heat fluxes (dashed black line, Fig. 7a) by a month or so, although the seasonal peaks are less strong in the export than the transformation. In contrast, the seasonal peaks in the OSNAP east dense water transport and overturning (red and black lines, Fig. 7a) are not as consistent in their timing and magnitude. The seasonal cycle of export in the

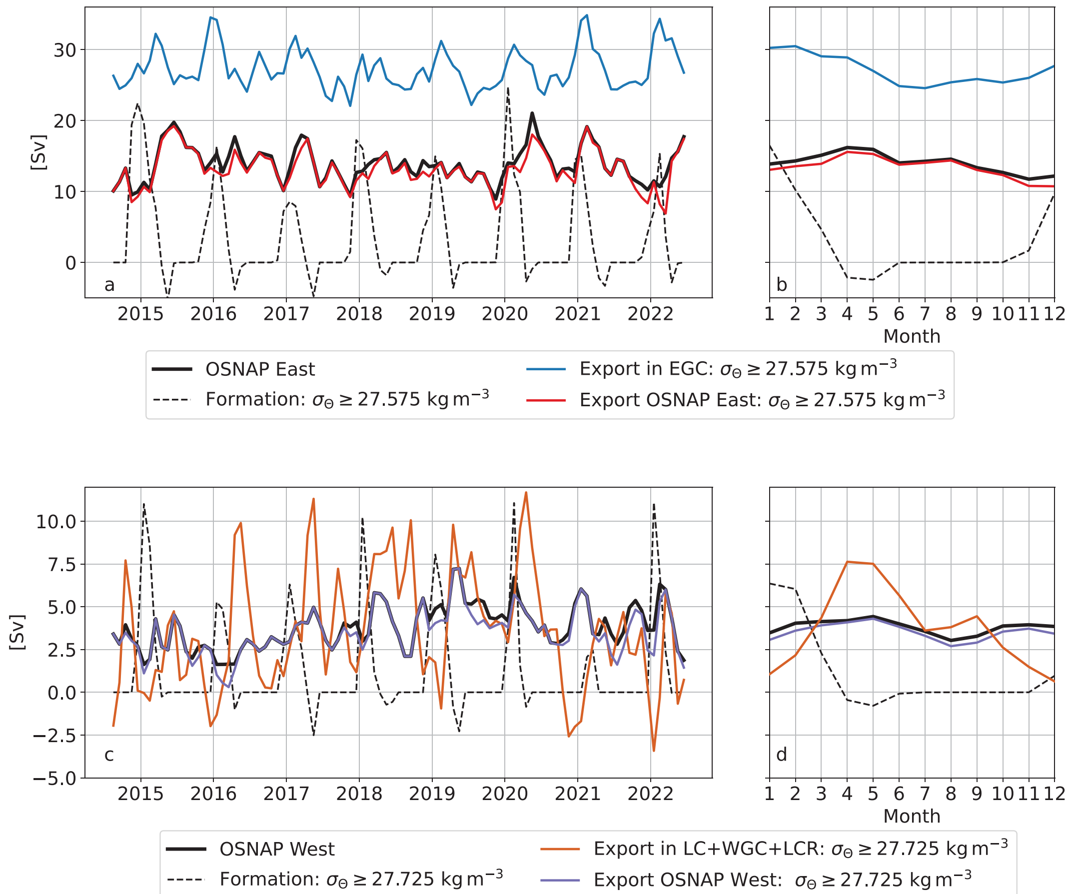

FIG. 7. Formation, export, and overturning. A comparison between dense water formation, export of dense water, and overturning variability at (a),(b) OSNAP east and (c),(d) OSNAP west for (a),(c) the full observational time series and (b),(d) the seasonal cycle. At OSNAP east, this comparison focuses on dense water from the mean density of maximum overturning ($\overline{\sigma}_{OV}^{east} = 27.575$ kg m^{-3}) to $\sigma = 28.0$ kg m^{-3}. At OSNAP west, this comparison focuses on the dense water from $\overline{\sigma}_{OV}^{west} = 27.725$ kg m^{-3} to $\sigma = 28.0$ kg m^{-3}. For these respective density ranges, formation in the respective basins by air–sea buoyancy fluxes is shown by the black dashed lines, and volume transport at OSNAP, representing export, is shown in the solid colored lines. Formation and export are compared to the overturning (solid black lines). At OSNAP east, dense water export is compared within the EGC and across the full eastern OSNAP basin. At OSNAP west, dense water export is compared within the combined LC and WGC and across the full western OSNAP basin.

EGC current (blue line, Fig. 7b) and OSNAP east (red line, Fig. 7b) is quite different. The export in the EGC is maximum in January/February, less than 1 month after the maximum in the transformation by air–sea buoyancy fluxes, although the export remains elevated until April. In contrast, the seasonal export over the full OSNAP east peaks in April/May. This implies that the seasonal (and interannual) variability of the diapycnal overturning at OSNAP east is not only driven by the export of recently formed dense water in the Irminger Sea but also by the accumulation of transport variability along the full length of OSNAP east.

At OSNAP west, we examine dense water formation and export between the mean $\overline{\sigma}_{OV}^{west} = 27.725$ kg m^{-3} and $\sigma = 28.0$ kg m^{-3} (Figs. 7c,d). We compare dense water formation, in the region between the OSNAP west array and the Davis Strait (black dashed line, Figs. 7c,d), to the diapycnal overturning (solid black line, Figs. 7c,d), the dense water transport in the West Greenland Current (WGC) and Labrador Current (LC, orange line, Figs. 7c,d), and the dense water transport across the full OSNAP west array (purple line, Figs. 7c,d).

At OSNAP west, we examine the net dense water transport in the WGC and LC. This choice is linked to the weaker diapycnal overturning in the western OSNAP basin, which means that the density of water flowing into the Labrador Sea via the WGC is close to the density of the water flowing out of the Labrador Sea via the LC (see Fig. 1b). Therefore, as we are interested in the net dense water export from the Labrador Sea, we consider the WGC and LC together.

The WGC (<47.6°W) and LC (>49.75°W) are defined based on the zonal extent of the time-mean northward and southward transport at the boundaries of the Labrador Sea (see the dashed vertical line in supplemental Figs. 2a and 3a). Within our definition of the LC, we also include the wind-driven recirculation present offshore of the LC, hereinafter

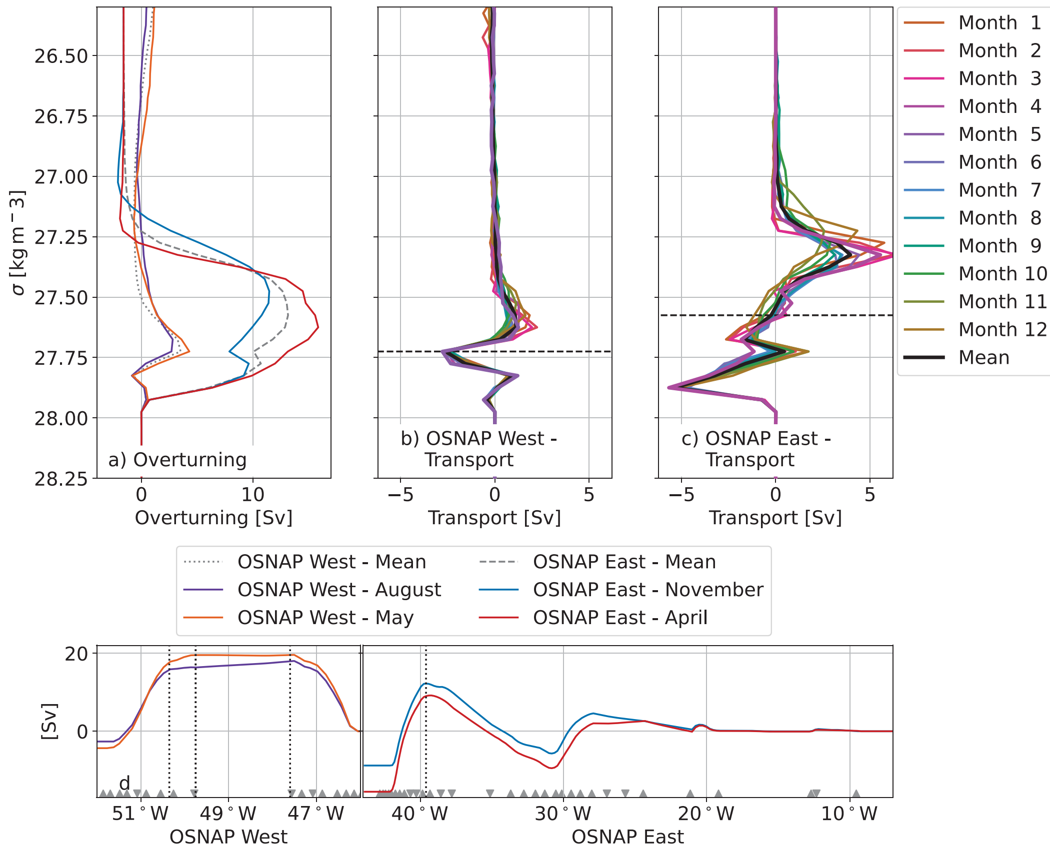

FIG. 8. Seasonal volume transport at OSNAP. (a) A comparison between the observed seasonal maximum and minimum overturning streamfunction at OSNAP east and OSNAP west, the seasonal volume transport in density space for (b) OSNAP west and (c) OSNAP east, and (d) the cumulative (from east to west) volume transport across each OSNAP basin from $\overline{\sigma}_{OV}^{west}$ to $\sigma = 28.0$ kg m^{-3} (OSNAP west) and from $\overline{\sigma}_{OV}^{east}$ to $\sigma = 28.0$ kg m^{-3} (OSNAP east) during the seasonal maximum and minimum overturning. The horizontal dashed lines in (b) and (c) indicate $\overline{\sigma}_{OV}^{west}$ and $\overline{\sigma}_{OV}^{east}$, respectively. The vertical dotted lines in (d) indicate (from west to east) the geographical boundaries used in Fig. 7, for the LC, LCR, WGC, and EGC. The gray triangles indicate the positions of moorings that make up the OSNAP array, where the inverted triangles indicate short moorings; see mooring positions in Fig. 1 for reference.

referred to as the Labrador Current recirculation (LCR; Lavender et al. 2000) evident in the OSNAP transports as a seasonal flow reversal between 50.35° and 49.75°W (supplemental Fig. 3a). The limits marking the extent of the WGC and the LC also demarcate the coverage of the OSNAP west moorings (gray triangles, supplemental Figs. 2 and 3).

The seasonal cycle (and interannual variability) of the diapycnal overturning agrees well with the integrated dense water export across OSNAP west, peaking in May, but with a weaker seasonal cycle than OSNAP east (black and purple lines, Figs. 7c,d). Dense water formation to the north of the OSNAP west array is maximum during January and February (dashed black line, Figs. 7c,d). However, the export of dense water in the WGC/LC peaks in April and May (orange line, Figs. 7c,d), with a seasonal amplitude that is ~4 times larger than the diapycnal overturning. This suggests that dense water export in the boundary current is compensated by dense water transport in the interior Labrador Sea, so that dense water export across OSNAP west bears little resemblance to the dense water export in the boundary currents. The seasonal cycle of export in the boundary currents (red line, Fig. 7d) is similarly much larger than the seasonal cycle across OSNAP west (blue line, Fig. 7d). Our analysis, therefore, does not support a strong lagged relationship between water mass formation and export in the boundary currents of the eastern and western OSNAP basins on these time scales.

The inability to establish a relationship between seasonal dense water formation and dense water export across OSNAP motivates us to examine the seasonal cycle of volume transport and how this varies along the OSNAP array. First, we compare the seasonality of volume transport in density space to the seasonal maximum and minimum of the diapycnal overturning streamfunction within each basin (Fig. 8). At OSNAP east, we show the diapycnal overturning streamfunction at its seasonal minimum (November, blue line, Fig. 8a) and maximum (April, red line, Fig. 8a). Between $\sigma \sim 27.75$ kg m^{-3} and $\sigma = 28.0$ kg m^{-3}, the profiles of the seasonal minimum and maximum diverge, caused by a net reversal in the dense water transport from southward to northward, centered at $\sigma = 27.75$ kg m^{-3}. Focusing on the seasonal cycle of

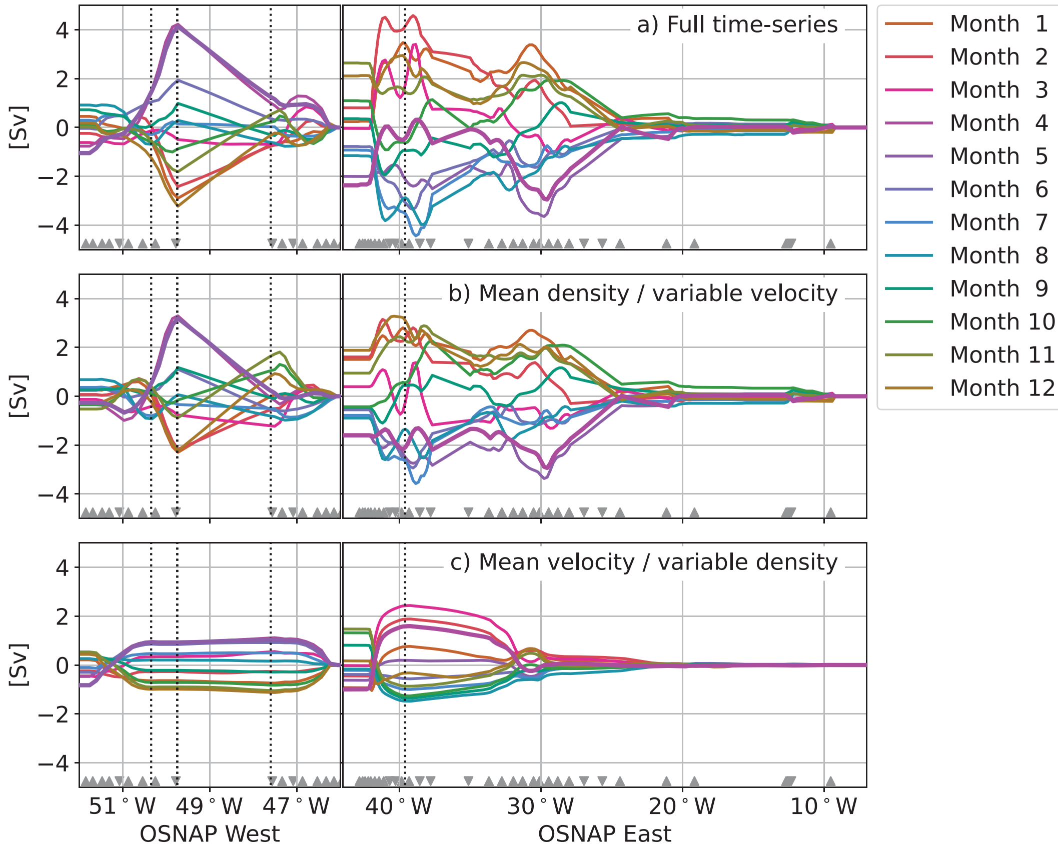

FIG. 9. Drivers of seasonal dense water transport variability. The anomaly of the observed monthly mean cumulative (from east to west) dense water volume transport with respect to the time mean from $\overline{\sigma}_{\mathrm{OV}}^{\mathrm{west}}$ to $\sigma = 28.0$ kg m^{-3} (OSNAP west) and from $\overline{\sigma}_{\mathrm{OV}}^{\mathrm{east}}$ to $\sigma = 28.0$ kg m^{-3} (OSNAP east). (a) Each month is shown by the colored lines. To separate the drivers of dense water transport variability, the cumulative volume transport variability is calculated (b) using the time-mean density while allowing velocity to vary and (c) using the time-mean velocity while allowing the density to vary. The gray triangles indicate the positions of moorings that make up the OSNAP array, where the inverted triangles indicate short moorings; see mooring positions in Fig. 1 for reference.

volume transport in density space at OSNAP east (Fig. 8c), we see that there is a net import (northward transport) of water at $\sigma \sim 27.75$ kg m^{-3} during most of the year except for April and May. This seasonal reversal results in both an increase in the total dense water (i.e., $\sigma > \overline{\sigma}_{\mathrm{OV}}^{\mathrm{east}}$) export and the diapycnal overturning. The cumulative dense water transport (integrated from east to west) for the seasonal minimum and maximum (blue and red lines, Fig. 8d; gray triangles indicate mooring positions) reveals that this is linked to a reversal in the dense water transport in the Iceland Basin and East Reykjanes Ridge Current, between 25° and 30°W (marked by a change in the slope of the cumulative transport), and by an increase in the southward transport of the EGC.

At OSNAP west, the seasonal minimum (August) and maximum (May) of the diapycnal overturning streamfunction diverges between $\overline{\sigma}_{\mathrm{OV}}^{\mathrm{west}}$ and $\sigma \sim 27.8$ kg m^{-3} due to a reduction in the net southward transport of dense water (purple and orange lines, respectively; Fig. 8a). This seasonal change in the net southward transport is evident in Fig. 8b near $\sigma \sim 27.75$ kg m^{-3}, which also highlights the apparent complexity of the net dense water transport into and out of the Labrador Sea. The seasonal contrast in the cumulative dense water transport at OSNAP west (Fig. 8d) is predominantly linked to an increase in the net southward transport of the LC system and is partly compensated for by an increase in the net northward transport of the WGC and a reversal of the net dense water transport within the interior of the Labrador Sea. In the LC, the seasonality of dense water export is dominated by the seasonal reversal of the LCR that transports dense water northward for much of the year except in April/May/June (Fig. 9, see also supplemental Figs. 3 and 8).

To further characterize the key regions of seasonal dense water transport variability along OSNAP east and west, we show the seasonal anomaly of the cumulative dense water transport (Fig. 9a), calculated by subtracting the time-mean cumulative dense water transport from the monthly mean cumulative dense water transport (i.e., subtracting the solid black line from the colored lines in supplemental Fig. 2). To qualitatively highlight the drivers of dense water transport, we also use the cumulative dense water transport calculated with a time-mean density field but with varying velocity (Fig. 9b) and with the time-mean velocity field but with varying density (Fig. 9c; see also supplemental Figs. 2–10). While density and velocity variability in this context will never be completely independent, the separation used here provides a good basis for a qualitative comparison. Along OSNAP east, this confirms that much of the cumulative seasonal dense water transport anomaly originates from the region between 25°W and the East Reykjanes Ridge (~30°W), and this is set by variability in the velocity field. Along OSNAP west, cumulative seasonal dense water transport anomalies arise from opposing variability in the interior of the Labrador Sea and LCR (see also supplemental Figs. 8–10) and are again driven by variability in the velocity field. Seasonal variability in the density field contributes to the seasonality of the EGC, WGC, and the LC. Combined, the dense water transport in the Iceland Basin, the East Reykjanes Ridge, the interior Labrador Sea, and the LCR is a key driver of diapycnal overturning seasonality. Notably, these sections of the mooring array are sparsely instrumented, and transport estimates here rely on hydrographic data. This is evident in the relative smoothness of the seasonal dense water transport anomaly in these regions compared to the sections of the OSNAP array that are more densely instrumented (supplemental Figs. 5 and 8).

In summary, at both OSNAP east and west, given the complex nature of the dense water inflows and outflows along the length of the mooring array, linking the export of recently formed dense water to the seasonality of the diapycnal overturning at OSNAP is challenging. At OSNAP east, the seasonal maximum in the dense water export of the EGC lags the peak in dense water formation by <1 month, but dense water export remains elevated through April. This elevated dense water export in the EGC, combined with a reversal of dense water transport within the Iceland Basin and East Reykjanes Ridge, leads to the peak in the diapycnal overturning during April. At OSNAP west, the net transport of dense water by the WGC and LC peaks in May, as does the diapycnal overturning, which both lag the peak in dense water formation by 4 months. However, the seasonal cycle of dense water transport is dominated by the seasonal reversal of the LCR and partly compensated by a reversal of dense water transport in the interior of the Labrador Sea. To fully account for the seasonal (and interannual) variability of the diapycnal overturning at OSNAP, dense water export must be integrated across the full width of the array, as opposed to only considering dense water export in the EGC and LC. Further, much of the diapycnal overturning seasonality arises from portions of the OSNAP array that are sparsely instrumented and transport estimates rely on hydrographic data.

4. Discussion and conclusions

In this study, we have used observations and model-based state estimates to understand the drivers of seasonal variability in the diapycnal overturning streamfunction at the OSNAP mooring array in the subpolar North Atlantic. We compared the diapycnal overturning as measured and simulated at the OSNAP mooring array to changes in the storage of water in density classes and the diapycnal water mass transformation by air–sea buoyancy fluxes and mixing. This highlights that seasonal variability in water mass transformation by surface buoyancy forcing and mixing in the region north of the OSNAP mooring array predominantly affects the storage of water in density classes with a seasonal cycle that is at least an order of magnitude larger than that of the overturning (Fig. 5).

Despite this discrepancy, we find a significant correlation between the maximum overturning streamfunction and the diapycnal transformation by air–sea buoyancy fluxes, where the air–sea fluxes lead the overturning by 4–5 months, in agreement with Fu et al. (2023). To determine if this lag is linked to the propagation time of dense water from its formation site to the OSNAP array, we compared the observed seasonal and interannual variability of dense water formation to the export of dense water and the diapycnal overturning as measured at OSNAP. This shows that the seasonal cycle of overturning at OSNAP is the product of imbalances in the inflows and outflows of dense water across the full OSNAP section, as opposed to the export of recently formed dense water in the East Greenland Current and Labrador Current.

In the eastern subpolar basin, dense water formation peaks in January, followed by a seasonal peak in dense water export in the East Greenland Current < 1 month later. The seasonal peak in the diapycnal overturning at OSNAP east in April is partly driven by an increase in dense water export in the East Greenland Current, which remains elevated following its seasonal maximum, and by an increase in the net southward transport of dense water within the Iceland Basin and East Reykjanes Current. In the Labrador Sea, the seasonal maximum in the net export of dense water within the West Greenland Current and Labrador Current lags the seasonal cycle in dense water formation by 3–4 months, but this variability is dominated by a seasonal reversal of the normally northward wind-driven recirculation adjacent to the Labrador Current. Further, the seasonal cycle of dense water export, and therefore the overturning, is modulated by compensating variability in the transport of dense water within the interior of the Labrador Sea.

We find that density variability along the OSNAP mooring array controls the seasonality of dense water transport within the East Greenland Current, the West Greenland Current, and the Labrador Current. Velocity variability controls the seasonality of dense water transport in the Iceland Basin, the East Reykjanes Ridge, the interior Labrador Sea, and the recirculation in the Labrador Current. As we have shown, dense water transport in these latter regions of the OSNAP mooring array is important for the seasonality of the diapycnal overturning, yet these regions are relatively sparsely instrumented and rely on hydrographic data to estimate transport. Float-, drifter-, and model-based studies have highlighted the complex circulation that overlays the basin-scale circulation of the North Atlantic Subpolar Gyre (including the recirculation in the Labrador Current) that is not fully resolved by the OSNAP mooring array (Lavender et al. 2000; Spall and Pickart 2003; Dengler et al. 2006; Zantopp et al. 2017). Further, Handmann et al. (2018) highlight that the location of the terminating mooring in the western portion of the OSNAP west array is critical for capturing the variability of the LCR. This raises the question of whether the current mooring configuration fully captures the recirculation in the Labrador Current and any other dense water recirculation pathways and, in the case of the former, whether the mooring data provide enough information to determine if there is actually a seasonal flow reversal or if there is instead a zonal expansion and contraction of the boundary current system.

Our water mass transformation analysis makes use of observations and a model-based state estimate, both of which have their own strengths and weaknesses. We use observations from the OSNAP mooring array in combination with gridded fields of temperature and salinity from hydrography and surface buoyancy fluxes from reanalysis. The model-based analysis uses ECCOv4r4 with fields of temperature, salinity, surface buoyancy forcing, and velocity fitted to observations. While the ECCOv4r4-based estimate of the diapycnal overturning at OSNAP does not exactly match the mooring-based observations, ECCOv4r4 is a useful tool for understanding water mass transformation budgets because ECCOv4r4 is dynamically and kinematically consistent and preserves property budgets exactly. On the other hand, the storage and residual terms estimated using observations also include errors linked to instrumentation, sampling, and interpolation, which impact our interpretation of these results. Further, as discussed above, we show that much of the seasonal (and interannual) variability is driven by dense water transport changes in regions of the OSNAP array with limited or no moorings, questioning the validity of the transport estimates in these regions.

We have, therefore, shown that the seasonal overturning variability measured at the OSNAP mooring array cannot be fully explained by seasonality in the formation of dense water by air–sea buoyancy fluxes and mixing, implying that at these time scales, the OSNAP mooring array does not capture changes in the diapycnal overturning circulation associated with dense water formation. Previous literature has shown that we should not necessarily expect the seasonal diapycnal overturning at OSNAP to reflect dense water formation because the residence time of water in the subpolar North Atlantic and Nordic seas is longer than the seasonal variability of water mass transformation in this region (Bower et al. 2009; MacGilchrist et al. 2021; Buckley et al. 2023; Tooth et al. 2023b). Instead, water mass transformation manifests as an annual breathing mode, where the forcing causes layers to expand and contract without either propagating elsewhere or impacting the overturning.

Our results suggest that the diapycnal overturning measured at the OSNAP mooring array represents seasonal density variability imprinted on the circulation of the North Atlantic Subpolar Gyre, where the overturning is a product of a complex interplay of inflows and outflows at the points where the array intersects the gyre (Tooth et al. 2023b). In other words, the recirculation of dense water within the subpolar gyre contaminates the relationship between the diapycnal overturning and the export of dense water via the main outflows of the subpolar basins. Previous studies have similarly highlighted how compensation between dense water inflows and outflows prevents the seasonality of dense water formation and export from imprinting onto the seasonality of the subpolar diapycnal overturning (Zantopp et al. 2017; Wang et al. 2021; Handmann et al. 2018). Further, Koman et al. (2024) also find that longer-term changes in the dense water transport of the deep western boundary current in the Irminger Sea do not lead to a similar decline in the diapycnal overturning at OSNAP. Our results, therefore, also point out the challenge of understanding how a collapse of the diapycnal overturning in the subpolar North Atlantic would manifest in the overturning estimated at OSNAP if transport variability on seasonal-to-interannual time scales is the product of aliased subpolar gyre variability driven by a combination of wind and buoyancy forcing (Spall and Pickart 2003; Kostov et al. 2021).

This work, therefore, raises the question of whether the Eulerian overturning as measured at the OSNAP mooring array is a suitable metric to quantify a buoyancy-driven AMOC in the subpolar North Atlantic associated with dense water export on shorter time scales. By design, the Eulerian overturning compares temporally disconnected inflows and outflows of light and dense water (i.e., the inflowing water is not the same as the outflowing water), and we show that the overturning measured at the OSNAP mooring array on seasonal time scales reflects seasonal imbalances in the inflows and outflows of dense water across the array. In models, an alternative framework would be a Lagrangian approach (Tooth et al. 2023a), in which water mass transformation is captured along the trajectories of water parcels, providing an estimate of the seasonal overturning that can be related directly to air–sea buoyancy fluxes and mixing. When using observations, this work highlights that the sources of short-term variability captured at moored arrays must be carefully considered before attributing the measured transport changes to diapycnal overturning variability linked to dense water formation and export.

Acknowledgments. D. G. E., N. P. H., and S. B. were funded by NERC research Grants CLASS (NE/R015953/1) and AtlantiS (NE/Y005589/1). O. J. T. is grateful for the financial support of the U.K. Natural Environment Research Council (NE/S007474/1) and the Atlantic Climate and Environment Strategic Science (AtlantiS) Grant (NE/Y005589/1). M. W. B. was funded by the NSF Physical Oceanography Program (2219707), NOAA ESS Program (NA20OAR4310396), and NASA Physical Oceanography Program (80NSSC20K0823).

Data availability statement. EN.4.2.2 data were obtained from https://www.metoffice.gov.uk/hadobs/en4/ and are Crown Copyright, Met Office, 2025, provided under a Non-Commercial Government Licence at https://www.nationalarchives.gov.uk/doc/non-commercial-government-licence/version/2/. ARMOR3D can be downloaded from the Copernicus Marine Service under the product identifier MULTIOBS_GLO_PHY_TSUV_3D_MYNRT_015_012 at https://data.marine.copernicus.eu/product/MULTIOBS_GLO_PHY_TSUV_3D_MYNRT_015_012/. ERA5 data were accessed from the Copernicus Data Store at https://doi.org/10.24381/cds.f17050d7. NCEP CFSv2 data were accessed from the NCAR/UCAR Research Data Archive at https://doi.org/10.5065/D69021ZF. JRA-55 data were accessed from the NCAR/UCAR Research Data Archive at https://doi.org/10.5065/D60G3H5B. The CMEMS Global Ocean Ensemble Reanalysis can be downloaded from the Copernicus Marine Service under the product identifier GLOBAL_REANALYSIS_PHY_001_031 at https://data.marine.copernicus.eu/product/GLOBAL_MULTIYEAR_PHY_ENS_001_031/. ECCOv4r4 was accessed via https://ecco-group.org/. OSNAP data are available via https://www.o-snap.org/data-access/. The Python-based code used to calculate water mass transformation is available here on GitHub at https://github.com/dgwynevans/wmt.

REFERENCES

Årthun, M., 2023: Surface-forced variability in the Nordic seas overturning circulation and overflows. *Geophys. Res. Lett.*, **50**, e2023GL104158, https://doi.org/10.1029/2023GL104158.

——, A. Brakstad, J. Dörr, H. L. Johnson, C. Mans, S. Semper, and K. Våge, 2025: Atlantification drives recent strengthening of the Arctic overturning circulation. *Sci. Adv.*, **11**, eadu1794, https://doi.org/10.1126/sciadv.adu1794.

Beaird, N., I. Fer, P. Rhines, and C. Eriksen, 2012: Dissipation of turbulent kinetic energy inferred from seagliders: An application to the eastern Nordic Seas overflows. *J. Phys. Oceanogr.*, **42**, 2268–2282, https://doi.org/10.1175/JPO-D-12-094.1.

Berglund, S., K. Döös, S. Groeskamp, and T. McDougall, 2023: North Atlantic Ocean circulation and related exchange of heat and salt between water masses. *Geophys. Res. Lett.*, **50**, e2022GL100989, https://doi.org/10.1029/2022GL100989.

Bower, A. S., M. S. Lozier, S. F. Gary, and C. W. Böning, 2009: Interior pathways of the North Atlantic meridional overturning circulation. *Nature*, **459**, 243–247, https://doi.org/10.1038/nature07979.

Brambilla, E., L. D. Talley, and P. E. Robbins, 2008: Subpolar mode water in the northeastern Atlantic: 2. Origin and transformation. *J. Geophys. Res.*, **113**, C04026, https://doi.org/10.1029/2006JC004063.

Broomé, S., L. Chafik, and J. Nilsson, 2020: Mechanisms of decadal changes in sea surface height and heat content in the eastern Nordic Seas. *Ocean Sci.*, **16**, 715–728, https://doi.org/10.5194/os-16-715-2020.

Brüggemann, N., and C. A. Katsman, 2019: Dynamics of downwelling in an eddying marginal sea: Contrasting the Eulerian and the isopycnal perspective. *J. Phys. Oceanogr.*, **49**, 3017–3035, https://doi.org/10.1175/JPO-D-19-0090.1.

Buckley, M. W., M. S. Lozier, D. Desbruyères, and D. G. Evans, 2023: Buoyancy forcing and the subpolar Atlantic meridional overturning circulation. *Philos. Trans. Roy. Soc.*, **A381**, 20220181, https://doi.org/10.1098/rsta.2022.0181.

Dengler, M., J. Fischer, F. A. Schott, and R. Zantopp, 2006: Deep Labrador Current and its variability in 1996–2005. *Geophys. Res. Lett.*, **33**, L21S06, https://doi.org/10.1029/2006GL026702.

Desbruyères, D. G., H. Mercier, G. Maze, and N. Daniault, 2019: Surface predictor of overturning circulation and heat content change in the subpolar North Atlantic. *Ocean Sci.*, **15**, 809–817, https://doi.org/10.5194/os-15-809-2019.

Dey, D., R. Marsh, S. Drijfhout, S. A. Josey, B. Sinha, J. Grist, and K. Döös, 2024: Formation of the Atlantic meridional overturning circulation lower limb is critically dependent on Atlantic-Arctic mixing. *Nat. Commun.*, **15**, 7341, https://doi.org/10.1038/s41467-024-51777-w.

Duchez, A., and Coauthors, 2016: Drivers of exceptionally cold North Atlantic Ocean temperatures and their link to the 2015 European heat wave. *Environ. Res. Lett.*, **11**, 074004, https://doi.org/10.1088/1748-9326/11/7/074004.

ECCO Consortium, Fukumori, I., O. Wang, I. Fenty, G. Forget, P. Heimbach, and R. M. Ponte, 2021b: Synopsis of the ECCO central production global ocean and sea-ice estimate, version 4 release 4. ECCO Consortium Rep., 17 pp., https://doi.org/10.5281/zenodo.4533349.

Evans, D. G., J. Toole, G. Forget, J. D. Zika, A. C. N. Garabato, A. J. G. Nurser, and L. Yu, 2017: Recent wind-driven variability in Atlantic water mass distribution and meridional overturning circulation. *J. Phys. Oceanogr.*, **47**, 633–647, https://doi.org/10.1175/JPO-D-16-0089.1.

——, N. P. Holliday, S. Bacon, and I. L. Bras, 2023: Mixing and air–sea buoyancy fluxes set the time-mean overturning circulation in the subpolar North Atlantic and Nordic Seas. *Ocean Sci.*, **19**, 745–768, https://doi.org/10.5194/os-19-745-2023.

Fer, I., G. Voet, K. S. Seim, B. Rudels, and K. Latarius, 2010: Intense mixing of the Faroe Bank Channel overflow. *Geophys. Res. Lett.*, **37**, L02604, https://doi.org/10.1029/2009GL041924.

Fischer, J., M. Visbeck, R. Zantopp, and N. Nunes, 2010: Interannual to decadal variability of outflow from the Labrador Sea. *Geophys. Res. Lett.*, **37**, L24610, https://doi.org/10.1029/2010GL045321.

Forget, G., J.-M. Campin, P. Heimbach, C. N. Hill, R. M. Ponte, and C. Wunsch, 2015: ECCO version 4: An integrated framework for non-linear inverse modeling and global ocean state estimation. *Geosci. Model Dev.*, **8**, 3071–3104, https://doi.org/10.5194/gmd-8-3071-2015.

Fox, A. D., N. J. Fraser, and S. A. Cunningham, 2025: Seasonality of meridional overturning in the subpolar North Atlantic: Density flux as a metric for understanding the Atlantic meridional overturning circulation. *Ocean Sci.*, **21**, 1735–1760, https://doi.org/10.5194/os-21-1735-2025.

Fu, Y., and Coauthors, 2023: Seasonality of the meridional overturning circulation in the subpolar North Atlantic. *Commun. Earth Environ.*, **4**, 181, https://doi.org/10.1038/s43247-023-00848-9.

——, and Coauthors, 2025: Characterizing the interannual variability of North Atlantic subpolar overturning. *Geophys. Res. Lett.*, **52**, e2025GL114672, https://doi.org/10.1029/2025GL114672.

Fukumori, I., O. Wang, I. Fenty, G. Forget, P. Heimbach, and R. M. Ponte, 2021: ECCO central estimate (version 4 release 4). Accessed 20 November 2020, https://ecco.jpl.nasa.gov/drive/files.

Good, S. A., M. J. Martin, and N. A. Rayner, 2013: EN4: Quality controlled ocean temperature and salinity profiles and monthly objective analyses with uncertainty estimates. *J. Geophys. Res. Oceans*, **118**, 6704–6716, https://doi.org/10.1002/2013JC009067.

Guinehut, S., A.-L. Dhomps, G. Larnicol, and P.-Y. Le Traon, 2012: High resolution 3-D temperature and salinity fields derived from in situ and satellite observations. *Ocean Sci.*, **8**, 845–857, https://doi.org/10.5194/os-8-845-2012.

Handmann, P., J. Fischer, M. Visbeck, J. Karstensen, A. Biastoch, C. Böning, and L. Patara, 2018: The deep western boundary current in the Labrador Sea from observations and a high-resolution model. *J. Geophys. Res. Oceans*, **123**, 2829–2850, https://doi.org/10.1002/2017JC013702.

Heimbach, P., and Coauthors, 2019: Putting it all together: Adding value to the global ocean and climate observing systems with complete self-consistent ocean state and parameter estimates. *Front. Mar. Sci.*, **6**, 55, https://doi.org/10.3389/fmars.2019.00055.

Hersbach, B., and Coauthors, 2021: ERA5 monthly averaged data on single levels from 1979 to present. Copernicus Climate Change Service (C3S) Climate Data Store (CDS), accessed 7 February 2021, https://doi.org/10.24381/cds.f17050d7.

Holliday, N. P., and Coauthors, 2020: Ocean circulation causes the largest freshening event for 120 years in eastern subpolar North

Atlantic. *Nat. Commun.*, **11**, 585, https://doi.org/10.1038/s41467-020-14474-y.

IOC, SCOR, and IAPSO, 2010: The International Thermodynamic Equation of Seawater—2010: Calculation and use of thermodynamic properties. Intergovernmental Oceanographic Commission, Manuals and Guides 56, 220 pp., https://www.teos-10.org/pubs/TEOS-10_Manual.pdf.

IPCC, 2021: *Climate Change 2021: The Physical Science Basis.* Cambridge University Press, 2392 pp., https://doi.org/10.1017/9781009157896.

JMA, 2013: JRA-55: Japanese 55-year Reanalysis, monthly means and variances. NSF National Center for Atmospheric Research, accessed 7 February 2021, https://doi.org/10.5065/D60G3H5B.

Kenigson, J. S., and M.-L. Timmermans, 2021: Nordic seas hydrography in the context of Arctic and North Atlantic Ocean dynamics. *J. Phys. Oceanogr.*, **51**, 101–114, https://doi.org/10.1175/JPO-D-20-0071.1.

Koman, G., A. S. Bower, N. P. Holliday, H. H. Furey, Y. Fu, and T. C. Biló, 2024: Observed decrease in deep western boundary current transport in subpolar North Atlantic. *Nat. Geosci.*, **17**, 1148–1153, https://doi.org/10.1038/s41561-024-01555-6.

Kostov, Y., and Coauthors, 2021: Distinct sources of interannual subtropical and subpolar Atlantic overturning variability. *Nat. Geosci.*, **14**, 491–495, https://doi.org/10.1038/s41561-021-00759-4.

Lavender, K. L., R. E. Davis, and W. B. Owens, 2000: Mid-depth recirculation observed in the interior Labrador and Irminger Seas by direct velocity measurements. *Nature*, **407**, 66–69, https://doi.org/10.1038/35024048.

Le Bras, I. A.-A., F. Straneo, J. Holte, M. F. de Jong, and N. P. Holliday, 2020: Rapid export of waters formed by convection near the Irminger Sea's western boundary. *Geophys. Res. Lett.*, **47**, e2019GL085989, https://doi.org/10.1029/2019GL085989.

Li, F., and Coauthors, 2021: Subpolar North Atlantic western boundary density anomalies and the meridional overturning circulation. *Nat. Commun.*, **12**, 3002, https://doi.org/10.1038/s41467-021-23350-2.

Lozier, M. S., and Coauthors, 2017: Overturning in the Subpolar North Atlantic Program: A new international ocean observing system. *Bull. Amer. Meteor. Soc.*, **98**, 737–752, https://doi.org/10.1175/BAMS-D-16-0057.1.

——, and Coauthors, 2019: A sea change in our view of overturning in the subpolar North Atlantic. *Science*, **363**, 516–521, https://doi.org/10.1126/science.aau6592.

MacGilchrist, G. A., H. L. Johnson, C. Lique, and D. P. Marshall, 2021: Demons in the North Atlantic: Variability of deep ocean ventilation. *Geophys. Res. Lett.*, **48**, e2020GL092340, https://doi.org/10.1029/2020GL092340.

Marsh, R., 2000: Recent variability of the North Atlantic thermohaline circulation inferred from surface heat and freshwater fluxes. *J. Climate*, **13**, 3239–3260, https://doi.org/10.1175/1520-0442(2000)013<3239:RVOTNA>2.0.CO;2.

Marshall, J., and K. Speer, 2012: Closure of the meridional overturning circulation through Southern Ocean upwelling. *Nat. Geosci.*, **5**, 171–180, https://doi.org/10.1038/ngeo1391.

——, D. Jamous, and J. Nilsson, 1999: Reconciling thermodynamic and dynamic methods of computation of water-mass transformation rates. *Deep-Sea Res. I*, **46**, 545–572, https://doi.org/10.1016/S0967-0637(98)00082-X.

Mercier, H., D. Desbruyères, P. Lherminier, A. Velo, L. Carracedo, M. Fontela, and F. F. Pérez, 2024: New insights into the eastern subpolar North Atlantic meridional overturning circulation from OVIDE. *Ocean Sci.*, **20**, 779–797, https://doi.org/10.5194/os-20-779-2024.

Oltmanns, M., J. Karstensen, G. W. K. Moore, and S. A. Josey, 2020: Rapid cooling and increased storminess triggered by freshwater in the North Atlantic. *Geophys. Res. Lett.*, **47**, e2020GL087207, https://doi.org/10.1029/2020GL087207.

Petit, T., M. S. Lozier, S. A. Josey, and S. A. Cunningham, 2020: Atlantic deep water formation occurs primarily in the Iceland Basin and Irminger Sea by local buoyancy forcing. *Geophys. Res. Lett.*, **47**, e2020GL091028, https://doi.org/10.1029/2020GL091028.

Saha, S., and Coauthors, 2012: NCEP Climate Forecast System version 2 (CFSv2) monthly products. NSF National Center for Atmospheric Research, accessed 7 February 2021, https://doi.org/10.5065/D69021ZF.

Spall, M. A., 2003: On the thermohaline circulation in flat bottom marginal seas. *J. Mar. Res.*, **61** (1), 1–25, https://doi.org/10.1357/002224003321586390.

——, 2004: Boundary currents and watermass transformation in marginal seas. *J. Phys. Oceanogr.*, **34**, 1197–1213, https://doi.org/10.1175/1520-0485(2004)034<1197:BCAWTI>2.0.CO;2.

——, and R. S. Pickart, 2001: Where does dense water sink? A subpolar gyre example. *J. Phys. Oceanogr.*, **31**, 810–826, https://doi.org/10.1175/1520-0485(2001)031<0810:WDDWSA>2.0.CO;2.

——, and ——, 2003: Wind-driven recirculations and exchange in the Labrador and Irminger Seas. *J. Phys. Oceanogr.*, **33**, 1829–1845, https://doi.org/10.1175/2384.1.

Stendardo, I., B. B. Nardelli, S. Durante, D. Iudicone, and D. Kieke, 2024: Interannual variability of subpolar mode water in the subpolar North Atlantic. *J. Geophys. Res. Oceans*, **129**, e2023JC019937, https://doi.org/10.1029/2023JC019937.

Straneo, F., 2006: On the connection between dense water formation, overturning, and poleward heat transport in a convective basin. *J. Phys. Oceanogr.*, **36**, 1822–1840, https://doi.org/10.1175/JPO2932.1.

Tooth, O. J., H. L. Johnson, and C. Wilson, 2023a: Lagrangian overturning pathways in the eastern subpolar North Atlantic. *J. Climate*, **36**, 823–844, https://doi.org/10.1175/JCLI-D-21-0985.1.

——, ——, ——, and D. G. Evans, 2023b: Seasonal overturning variability in the eastern North Atlantic subpolar gyre: A Lagrangian perspective. *Ocean Sci.*, **19**, 769–791, https://doi.org/10.5194/os-19-769-2023.

Våge, K., and Coauthors, 2011: The Irminger Gyre: Circulation, convection, and interannual variability. *Deep-Sea Res. I*, **58**, 590–614, https://doi.org/10.1016/j.dsr.2011.03.001.

Verezemskaya, P., B. Barnier, S. K. Gulev, S. Gladyshev, J.-M. Molines, V. Gladyshev, J.-M. Lellouche, and A. Gavrikov, 2021: Assessing eddying (1/12°) ocean reanalysis GLORYS12 using the 14-yr instrumental record from 59.5°N section in the Atlantic. *J. Geophys. Res. Oceans*, **126**, e2020JC016317, https://doi.org/10.1029/2020JC016317.

Walin, G., 1982: On the relation between sea-surface heat flow and thermal circulation in the ocean. *Tellus*, **34** (2), 187–195, https://doi.org/10.3402/tellusa.v34i2.10801.

Wang, H., J. Zhao, F. Li, and X. Lin, 2021: Seasonal and interannual variability of the meridional overturning circulation in the subpolar North Atlantic diagnosed from a high resolution reanalysis data set. *J. Geophys. Res. Oceans*, **126**, e2020JC017130, https://doi.org/10.1029/2020JC017130.

Xu, X., P. B. Rhines, and E. P. Chassignet, 2018: On mapping the diapycnal water mass transformation of the upper North Atlantic Ocean. *J. Phys. Oceanogr.*, **48**, 2233–2258, https://doi.org/10.1175/JPO-D-17-0223.1.

Zantopp, R., J. Fischer, M. Visbeck, and J. Karstensen, 2017: From interannual to decadal: 17 years of boundary current transports at the exit of the Labrador Sea. *J. Geophys. Res. Oceans*, **122**, 1724–1748, https://doi.org/10.1002/2016JC012271.

Zou, S., T. Petit, F. Li, and M. S. Lozier, 2024: Observation-based estimates of water mass transformation and formation in the Labrador Sea. *J. Phys. Oceanogr.*, **54**, 1411–1429, https://doi.org/10.1175/JPO-D-23-0235.1.